




Size, structure, and luminescence of $\text{Nd}_2\text{Zr}_2\text{O}_7$ nanoparticles by molten salt synthesis

Jose P. Zuniga¹, Santosh K. Gupta^{1,2}, Maya Abdou¹, Héctor A. De Santiago¹, Alexander A. Puretzky³, Melonie P. Thomas⁴, Beth S. Guiton⁴, Jue Liu⁵, and Yuanbing Mao^{1,6,*} 

¹ Department of Chemistry, University of Texas Rio Grande Valley, 1201 West University Drive, Edinburg, TX 78539, USA

² Radiochemistry Division, Bhabha Atomic Research Centre, Trombay, Mumbai 400085, India

³ Center for Nanophase Materials Sciences, Oak Ridge National Laboratory, Oak Ridge, TN 37831, USA

⁴ Department of Chemistry, University of Kentucky, 505 Rose Street, Lexington, KY 40506, USA

⁵ Neutron Science Directorate, Oak Ridge National Laboratory, 1 Bethel Valley Rd, Oak Ridge, TN 37831, USA

⁶ School of Earth, Environmental, and Marine Sciences, University of Texas Rio Grande Valley, 1201 West University Drive, Edinburg, TX 78539, USA

Received: 11 March 2019

Accepted: 3 June 2019

© Springer Science+Business Media, LLC, part of Springer Nature 2019

ABSTRACT

Pyrochlore materials with novel properties are in demand with multifunctional applications such as optoelectronics, scintillator materials, and theranostics. Many reports have already indicated the importance of the synthesis technique for $\text{Nd}_2\text{Zr}_2\text{O}_7$ (NZO) nanoparticles (NPs); however, no explanation has been provided for the reason behind the nature of its phase selectivity. Here, we have explored the structural and optical properties of the NZO NPs synthesized by a molten salt synthesis method. We have synthesized size-tunable NZO NPs and correlated the particle size with their structural behavior and optical performance. All NZO NPs are stabilized in defect fluorite phase. Neutron diffraction provided insight on the behavior of oxygen in the presence of heavy atoms. We have collected bright amalgam of blue and green emission on UV irradiation due to the presence of oxygen vacancies from these NPs. We have carried out in situ XRD and Raman investigations to observe the temperature-induced phase transformation in a controlled argon environment. Interestingly, we have not observed phase change for the molten salt synthesized fluorite NZO NPs; however, we observed phase transformation from a precursor stage to pyrochlore phase by in situ XRD directly. These observations provide a new strategy to synthesize nanomaterials phase-selectively for a variety of applications in materials science.

Address correspondence to E-mail: yuanbing.mao@utrgv.edu

Introduction

Pyrochlore materials with $A_2B_2O_7$ composition have been the focal point of research recently because of their unique properties such as high dielectric constant [1], low thermal [2], oxygen ion conductivity [3], high radiation stability [4], structural flexibility [5, 6], and order–disorder phase transition, etc. [7]. This leads them to have many applications in different technologically advanced areas such as luminescence host, self-activated phosphors, scintillators, nuclear waste hosts, actinide speciation, solid oxide fuel cell, thermal barrier coatings, catalysis, and magnetism, etc. [5, 8–19]. Among different pyrochlores, $Nd_2Zr_2O_7$ (NZO) stands out with its fascinating properties as an ideal candidate for a variety of applications such as solid-state laser [16], photocatalyst [20], host for minor actinides transmutation [21], magnets [22], and coatings [23], etc. Pyrochlore compounds are known to exist in two different structures, fluorite ($Fm\bar{3}m$) and ideal pyrochlore ($Fd\bar{3}m$) [24, 25]. For a given $A_2B_2O_7$ composition, its relative stability depends upon the ionic radius ratio of r_A/r_B [26]. Based on its radius ratio, NZO has a r_A/r_B value of 1.12 and is expected to be stabilized in disorder fluorite structure. One can calculate DFT-based cohesive energy for both of these structures to predict the stability of $A_2B_2O_7$ compounds [27]. For example, it was predicted that the ideal pyrochlore ($Fd\bar{3}m$) structure is favorable with respect to the fluorite ($Fm\bar{3}m$) structure for bulk $Gd_2Hf_2O_7$. Jiang et al. [28] and Li et al. [29] have shown that the ground state structure of $Gd_2Hf_2O_7$ is ideal pyrochlore. They have also calculated ideal pyrochlore to fluorite transformation temperatures for several $A_2B_2O_7$ compounds. Moreover, there are studies on the stability of NZO at high temperature and high pressure. For example, Xiao et al. [30] have carried out theoretical calculations on NZO and theoretically predicted phase transformations to the defect-cotunnite structure at pressures of 22, 20, and 18 GPa. Payne et al. [31] have carried out reverse Monte Carlo (RMC) modelling study of $Nd_2Zr_2O_7$ to predict that fluorite structure is adopted by the sample prepared at 800 °C from an amorphous precursor and have supported their predictions by X-ray, neutron, and electron diffraction techniques. They also demonstrated a phase transition to a pyrochlore-type structure after annealing the sample at 1000 °C.

Structure plays an important role in dictating the properties of a material while its synthesis method could determine the structure and hence the property. Several techniques have been applied to prepare NZO powders such as solid state [32], complex precipitation [33], coprecipitation [23], combustion [16], sol–gel [34], citrate precursor [35], aqueous chemical synthesis [36], and modified Pechini route [20], etc. Solid-state route requires high temperature and long time and results in agglomerated (fused) or aggregated (necked) particles. Combustion synthesis results in evolution of CO_2 , CO, and NO_x , which can raise safety concerns. It may also need high heating temperature for pure and crystalline nanoparticles of some pyrochlore materials which may lead to the evaporation of salt [33]. As found in the literature, solid-state ceramic route leads to ideal pyrochlore NZO that undergoes phase transition to fluorite phase upon annealing at 2300 °C [37]. In another report, NZO stabilizes in fluorite phase when heat-treated at 900 °C but undergoes phase transformation to ideal pyrochlore phase at 1000–1400 °C [36].

At the meantime, there is ambiguity in deciding the structure of NZO [34, 35, 38, 39]. Lee et al. [35]. and Bhattacharya et al. [34] reported the stabilization of NZO as fluorite phase when synthesized at 750 and 700 °C, respectively. On the other hand, Zhang and group [38] reported poor crystalline pyrochlore phase of NZO synthesized at 600 °C. Rao et al. [39] were not certain about the structure of NZO synthesized at 500 °C. Such structural ambiguity is attributed to nature/crystallinity of samples and small size of nanoparticles, which leads to broad XRD pattern. In addition, the close structural relationship between fluorite and pyrochlore does not make the crystal distinction easy. The pyrochlore diffraction pattern consists of strong reflections (related to the fluorite substructure) and weaker pyrochlore superstructure reflections resulting from the ordering of cations and anions.

There is no report on the development of NZO nanostructures using molten salt synthesis (MSS) wherein reactants get dissolved in a molten salt flux that assists in mixing and diffusion of reactant molecules, and products are formed at relatively low temperature [40, 41]. In addition, product formation takes place at relatively mild conditions, and there is no requirement of sophisticated reaction vessels or expensive raw materials. For many applications, nanoparticles with certain size range are required.

MSS method also allows the tuning of nanoparticle size by varying the MSS processing time [42], processing temperature, and coprecipitating pH [9], etc. Here, we have adopted the novel MSS approach to make NZO NPs with different sizes by varying the coprecipitating pH and exploring their structural and luminescent properties. Moreover, we have investigated the structural evolution of NZO NPs with in situ X-ray diffraction (XRD) and Raman spectroscopy by thermal treatment of the formed NZO NPs and their corresponding precursor. We have found phase selectivity depending on the synthesis procedures of NZO. While using the MSS method, it was found that the formed NZO NPs prefer the defect fluoride structure while direct annealing of the coprecipitated precursor prefers the formation of more order pyrochlore phase. This investigation provides insight on the phase stabilization of $\text{Nd}_2\text{Zr}_2\text{O}_7$ NPs and the effect of coprecipitation pH on their structural and optical properties.

Experimental

Synthesis

In this work, the NZO NPs were prepared via a combined coprecipitation and MSS technique. In the coprecipitation step, ammonium hydroxide aqueous solution (NH_4OH , 28–30%) was diluted to varying concentrations (0.75, 1.5, 3.0, 4.5, and 6.0%) and used as the precipitant. Stoichiometric amounts of the composing elements of neodymium(III) nitrate hexahydrate ($\text{Nd}(\text{NO}_3)_3 \cdot 6\text{H}_2\text{O}$, 99.9%) and zirconium(IV) oxynitrate hydrate ($\text{ZrO}(\text{NO}_3)_2 \cdot x\text{H}_2\text{O}$) were measured and dissolved in 200 mL of distilled water (18.2 M Ω at 25 °C). The solution was then titrated with the NH_4OH solution with different concentrations. The formed precipitate was washed with DI water until it was neutral and then vacuum filtrated and dried. For the MSS step, the obtained complex single-source precursor was mixed and grinded with sodium nitrate (NaNO_3 , 98%) and potassium nitrate (KNO_3 , 99%) with a stoichiometric ratio of (1:30:30) until a fine powder was obtained, which was then annealed at 650 °C for 6 h, with ramp-up and ramp-down rates of 10 °C/min. The final NPs were washed with DI water several times and dried at 90 °C overnight. The change of the NH_4OH concentration is reflected in the change of the coprecipitating pH

value where there is a progressive increase in the pH value as reported in our earlier work⁹. The five NZO samples prepared from the mentioned NH_4OH solution with different concentrations are designated as NZO-S0.75, NZO-S1.5, NZO-S3, NZO-S4.5, and NZO-S6.

Characterization

The obtained NZO NPs were characterized using X-ray diffraction (XRD), neutron diffraction (ND), Fourier transformed infrared (FTIR) spectroscopy, Raman spectroscopy, scanning electron microscopy (SEM), transmission electron microscopy (TEM), energy-dispersive X-ray spectroscopy (EDS), and photoluminescence (PL) spectroscopy.

XRD was used to confirm the purity and crystallinity of the NZO samples. The XRD patterns were recorded on a BRUKERTM D8 X-ray Diffractometer with a Cu $K_{\alpha 1}$ radiation ($\lambda = 0.15406$ nm, 40 kV, 40 mA), with a scanning range from 10° to 90°, using a scanning mode of 2θ , a scanning rate of 1.0° min⁻¹, and scanning step size of 0.04°.

Powder ND patterns were collected for the NZO-S1.5 NPs using Nanoscale-Ordered Materials Diffractometer (NOMAD) at the Spallation Neutron Source (SNS) of Oak Ridge National Laboratory, United States [43]. For the current experiment, about 5.0 g powder sample of the NZO-S1.5 NPs was loaded into a 3-mm quartz capillary. Two 30 min scans were collected for the powder sample and then summed together to improve statistics. The positions of detectors were calibrated using scattering from a diamond powder standard. The corresponding background (empty container) was then subtracted, and neutron powder diffraction data were normalized against the scattering of a vanadium rod. Rietveld refinement of the average structure was carried out using TOPAS academic version 6. The conversion from time-of-flight to d-spacing was done using a second-order polynomial function ($\text{TOF} = d_0 + dfc \cdot d + dfa \cdot d^2$) calibrated from a NIST Si 640e standard sample. During the refinement, d_0 and dfc were fixed to the values refined from Si standard while dfa was allowed to vary to account for the sample displacement. For the low angle bank ($2\theta = 32^\circ$), d_0 was also allowed to vary to account for the potential absorption induced peak shift. The diffraction peak shapes were primarily modeled using a back to back exponential function (asymmetrical peak contribution from the instrument)

with the convolution of a pseudo-Voigt function (contains both instrument and sample broadening contribution, please note microstrain and size broadening were not refined separately for this study).

FTIR spectra were collected using a FTIR ALPHA II's Platinum ATR single reflection diamond ATR module. The morphology and microstructure of the NPs were assessed using a Carl Zeiss sigma VP SEM with a field emission gun operated at 5 kV. TEM and EDS characterization was performed using HF3300, cold-FEG 300 kV TEM/STEM equipped with a Bruker XFlash 60 mm² SDD-type detector. The Raman spectra were obtained using a Raman spectrometer (Renishaw-2000, Renishaw, Inc.) with an Ar ion laser (514 nm, 5 mW). PL emission and excitation spectra were recorded on an Edinburgh Instrument FLS 980 fluorometer system equipped with both pulsed and steady state xenon lamp source having a frequency range of 1–100 Hz.

In situ XRD measurement was carried out on a PANalytical XPert PRO equipment having Cu K-alpha source (wavelength 1.540598 Å). It is coupled with 60 kV and 55 mA MRI Heating Chamber for PreFIX with a Pt heater element 10 mm width. The measurements were collected in a Theta-Theta configuration with radius beam of 240 mm and step size of 0.01°.

In situ Raman measurements were performed using a custom-built micro-Raman setup. The samples were placed in a high-temperature microscope stage (TS-1500, Linkam) and were excited with a continuous wave (CW) diode-pumped solid-state laser (Excelsior, Spectra Physics, 532 nm) through an upright microscope using a 50 × long-working distance objective with NA (numeric aperture) = 0.5. The typical incident laser power on a sample was maintained at ~ 100 μW. The scattered Raman light was analyzed by a spectrometer (Spectra Pro 2300i, Acton, $f = 0.3$ m) that was coupled to the microscope and equipped with an 1800 grooves/mm grating and a CCD camera (Pixis 256BR, Princeton Instruments).

Result and discussion

Phase and structural analysis: XRD, Raman, and FTIR spectroscopy

All the XRD patterns of our NZO NPs (Fig. 1a) match closely with those from pure Nd₂Zr₂O₇ [13]. The XRD patterns also revealed well-defined peaks with good

degree of crystallinity. There is no change of the XRD patterns as a function of the coprecipitating NH₄OH concentration and pH value.

It is difficult to identify the crystal structure of NZO based on XRD due to the close proximity in disordered fluorite ($Fm\bar{3}m$ space group) and order pyrochlore ($Fd\bar{3}m$ space group) structures. Because of its high sensitivity toward M–O vibrations, Raman spectroscopy is an indispensable tool to differentiate these two phases. Based on point group theory, the ideal pyrochlore phase of A₂B₂O₇ compounds consists of six vibrational bands in the range of 200–1000 cm^{−1}, which are attributed to $\Gamma_{\text{pyr}} = A_{1g} + E_g + 4F_{2g}$ [44, 45]. On the other hand, defect fluorite structure mainly consists of a single broad vibrational peak attributed to $\Gamma_{\text{flu}} = F_{2g}$ due to the random distribution of oxygen ions over eight available positions, which cause large structural disordering. Regarding the ionic radius ratio r_A/r_B as a critical parameter in deciding the structure of pyrochlore lattice, it is reported that a disorder fluorite is favored when r_A/r_B is less than 1.46, whereas order pyrochlore is the prevalent structure when r_A/r_B is more than 1.46 [46]. NZO is stabilized in an disorder fluorite structure because of $r(\text{Nd}^{3+}) = 1.106$ Å and $r(\text{Zr}^{4+}) = 0.983$ Å, giving a $r_{\text{Nd}^{3+}}/r_{\text{Zr}^{4+}} = 1.12$. The Raman spectra of all five NZO NPs displayed a broadband peaking around 323 cm^{−1} due to F_{2g} vibration of the disordered fluorite structure (Fig. 1b). The small shoulder band around 505 cm^{−1} can be attributed to the A_{1g} vibration mode that gives important information of the force constant provided by the oscillations of La–O and Hf–O [18, 47]. The peak at 644 cm^{−1} can be attributed to the F_{2g} vibrational mode corresponding to the stretching of the Hf–O bond. Usually, the 505 cm^{−1} peak is present in the pyrochlore phase indicating certain order in the NZO NPs [48]. However, the characteristics of the A_{1g} peak are minimum compared to the strong band at 323 cm^{−1} which depicts a dominant defect fluorite structure. Change of the coprecipitating NH₄OH concentration did not alter the basic fluorite network of NZO.

From the FTIR spectra of the NZO NPs (Fig. 1c), the broadband peak located around 3400 cm^{−1} is attributed to the stretching mode of water molecules which are absorbed on the surface of the NZO NPs [49]. The relatively sharper peak around 1330–1500 cm^{−1} is due to the bending vibration of

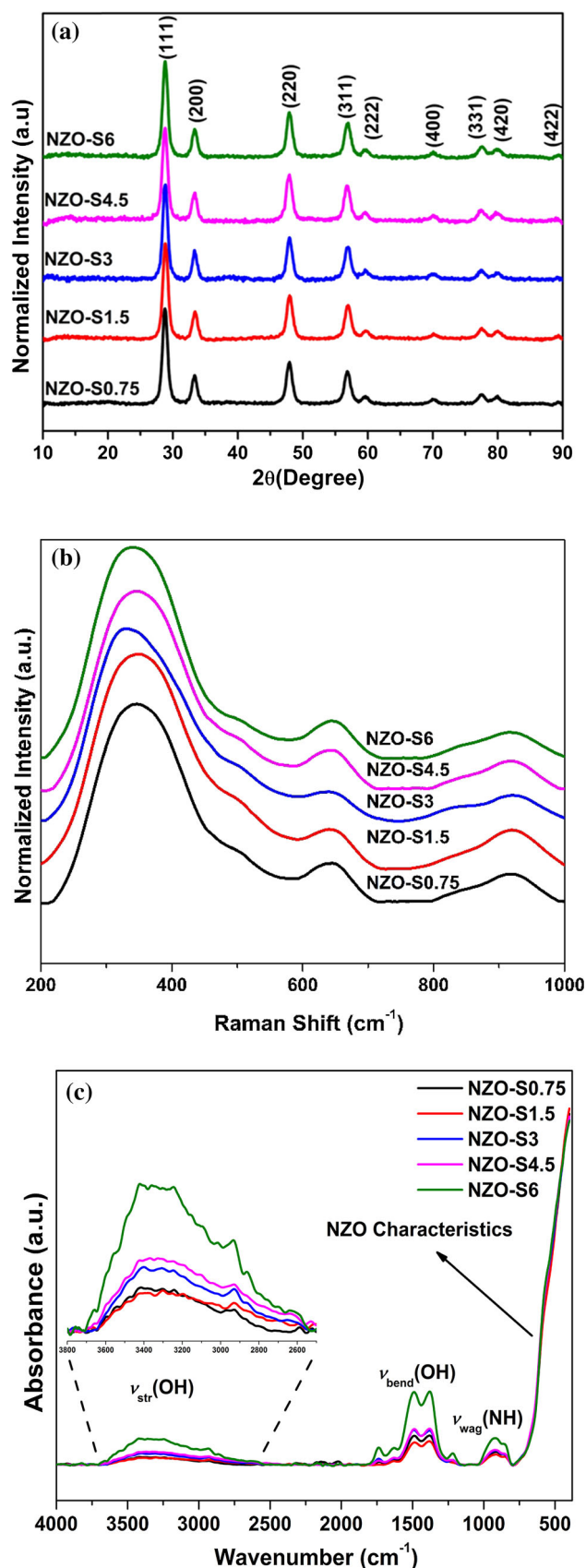


Figure 1 a XRD patterns, b Raman spectra, and c FTIR spectra of the NZO NPs.

OH bond [8]. The IR absorption band at $840\text{--}920\text{ cm}^{-1}$ is attributed to wagging vibration of NH band. The characteristic peak of the neodymium zirconate is located at 504 cm^{-1} [50].

Neutron powder diffraction studies

As a medium resolution diffractometer, NOMAD operates with a large bandwidth of neutron energies with a sensitive detector for structural determination of local order in crystalline and amorphous materials [51]. Here, we used this important tool to explore the behavior of oxygen in the presence of heavy atoms. In addition, to investigate site occupancy, we refined crystal structure of the $\text{Nd}_2\text{Zr}_2\text{O}_7$ NPs using Rietveld analysis. Figure 2a shows the refined neutron powder diffraction patterns of the NZO-S1.5 NPs. In the figure, the black line represents the observed normalized intensity, the red line represents the calculated intensity from the structure model, and the blue line represents the difference between the observed and calculated intensity. The final R_{wp} value is 1.93%, and Gof (Goodness of fit = $R_{\text{wp}}/R_{\text{exp}}$) is 2.74. Table 1 shows the Rietveld refinement structure. Nd atoms were located at (0, 0, 0) at 16c site while Zr atoms were refined at (1/2, 1/2, 1/2) at 16d site. In addition, O-O_1 was located at (1/8, 1/8, 1/8) at 8a site and O-O_2 was attributed to (3/8, 1/8, 1/8) at 48f site. Over all, the refinement indicated that the $\text{Nd}_2\text{Zr}_2\text{O}_7$ NPs was found to have a disordered fluorite type ($Fm\bar{3}m$ space group) structure with oxygen vacancies distributing over 8a and 48f sites at room temperature [52]. Figure 2b shows the Rietveld refined crystal structure of the NZO NPs. It is clearly seen that Nd exists in an 8-coordinated ideal cube geometry, whereas Zr is in a 6-coordinated distorted octahedral geometry. This is the characteristics of a typical defect fluorite structure [53].

Morphology analysis: SEM and TEM

As shown in the SEM Figures (Fig. 3a–e), the NZO NPs synthesized from low NH_4OH concentration are mostly spherical but are clustered together. With increasing NH_4OH concentration, the number of uniform spherical NPs is decreased, and the particles

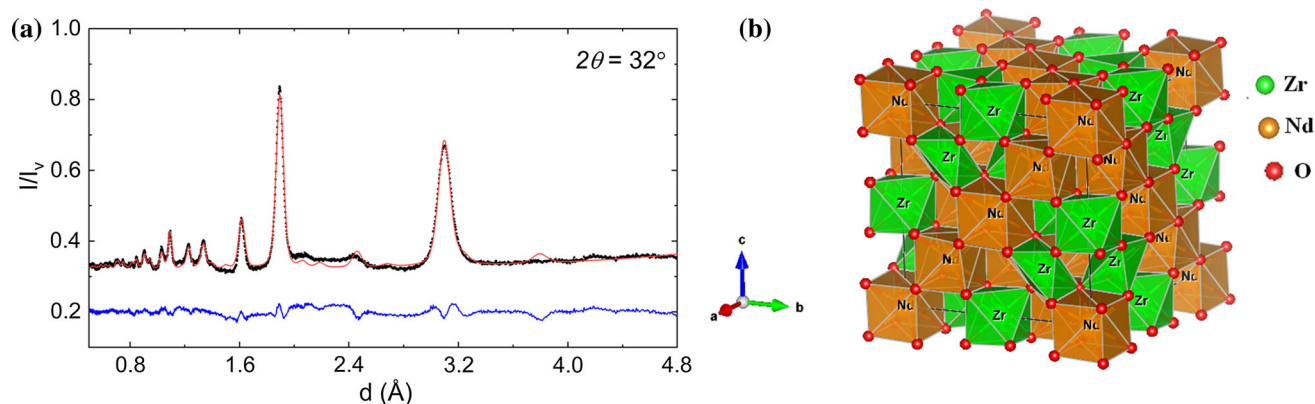


Figure 2 **a** Neutron powder diffraction pattern, **b** refined crystal structure of the $\text{Nd}_2\text{Zr}_2\text{O}_7\text{-S1.5}$ NPs.

Table 1 Refined structure of the $\text{Nd}_2\text{Zr}_2\text{O}_7\text{-S1.5}$ NPs from the powder ND data with the numbers within the brackets as the refined errors

Atom	Wyck.	x	y	z	Occ.	$B_{\text{eq}} (\text{\AA}^2)$
Zr1	16d	0.50000	0.50000	0.50000	1	1.10 (6)
Nd	16c	0.00000	0.00000	0.00000	1	0.90 (5)
O1	8a	0.12500	0.12500	0.12500	1	3.64 (5)
O2	48f	0.3947 (2)	0.12500	0.12500	1	3.64 (5)

Refined $a = 10.7019(13) \text{ \AA}$

become more irregular and agglomerated. The presence of excess hydroxyl group on the amorphous complex single-source precursor particles coprecipitated from NH_4OH solution with high concentration serves as a co-space-filling template, which can induce the final NZO NPs to grow in specific directions. Hence, irregular microstructures and highly agglomerated particle-like structures were formed. Also, there is a progressing increase in the average particle size of these NPs from ~ 25 to 53 nm when the coprecipitating NH_4OH concentration is increased from 0.75 to 6.0%.

Low-resolution TEM image of the NZO NPs (Fig. 4a) shows the monodispersed NZO NPs with spherical morphology. The high-resolution TEM image (Fig. 4b,c) shows high crystallinity of MSS-synthesized NZO NPs with well-defined lattice fringes with 3.116 \AA interplanar spacing, which corresponds to $\{222\}$ of cubic $\text{Nd}_2\text{Zr}_2\text{O}_7$. The details of the filtering process involved in elucidating image Fig. 4c are explained in one of our early publications [54].

Energy-dispersive spectroscopic (EDS) analysis (Fig. 5) clearly confirms the presence of Nd, Zr, and

O in the NZO-S6 NPs. As shown in the EDS mapping images (Fig. 5b), Nd, Zr, and O elements were distributed uniformly in the NZO lattice.

PL spectroscopy

The excitation spectra of the NZO NPs at λ_{em} of 450 nm (Fig. 6a) displayed a broadband peaking around 281 nm , which could be attributed to intrinsic $\text{O} \rightarrow \text{Zr}$ charge transfer. The weak peak around 335 nm can be attributed to some oxygen-related structural defects. The emission spectra recorded with λ_{ex} of 281 nm (Fig. 5b) showed two intense bands in the visible region: one at 450 nm (blue) and the other at 554 nm (green).

The presence of such multicolored (blue and green) spectral feature in functional material is typical of defect-induced emission wherein large number of intermediate levels that reside between the band gap are involved in relaxation process [55]. Normally, defects are present in abundance in nanostructured materials depending on synthesis techniques. There are different categories of point defects such as vacancies (cation/anion), antisite defects, interstitials, and structural defects, etc. Oxygen vacancies are the most common defects responsible for visible emission in activator-free materials like perovskites, spinels, and pyrochlores, etc. [12, 56–58]. Our results are in agreement with PL properties of the gel-combustion synthesized nanostructured NZO reported by one of the co-authors, where different sized NPs were achieved by thermal treatment [19]. Based on our neutron diffraction data, the NZO NPs were found to have a disordered fluorite ($Fm\bar{3}m$ space group) structure with oxygen vacancies (OV) distributing over 8a and 48f sites at room temperature. Moreover,

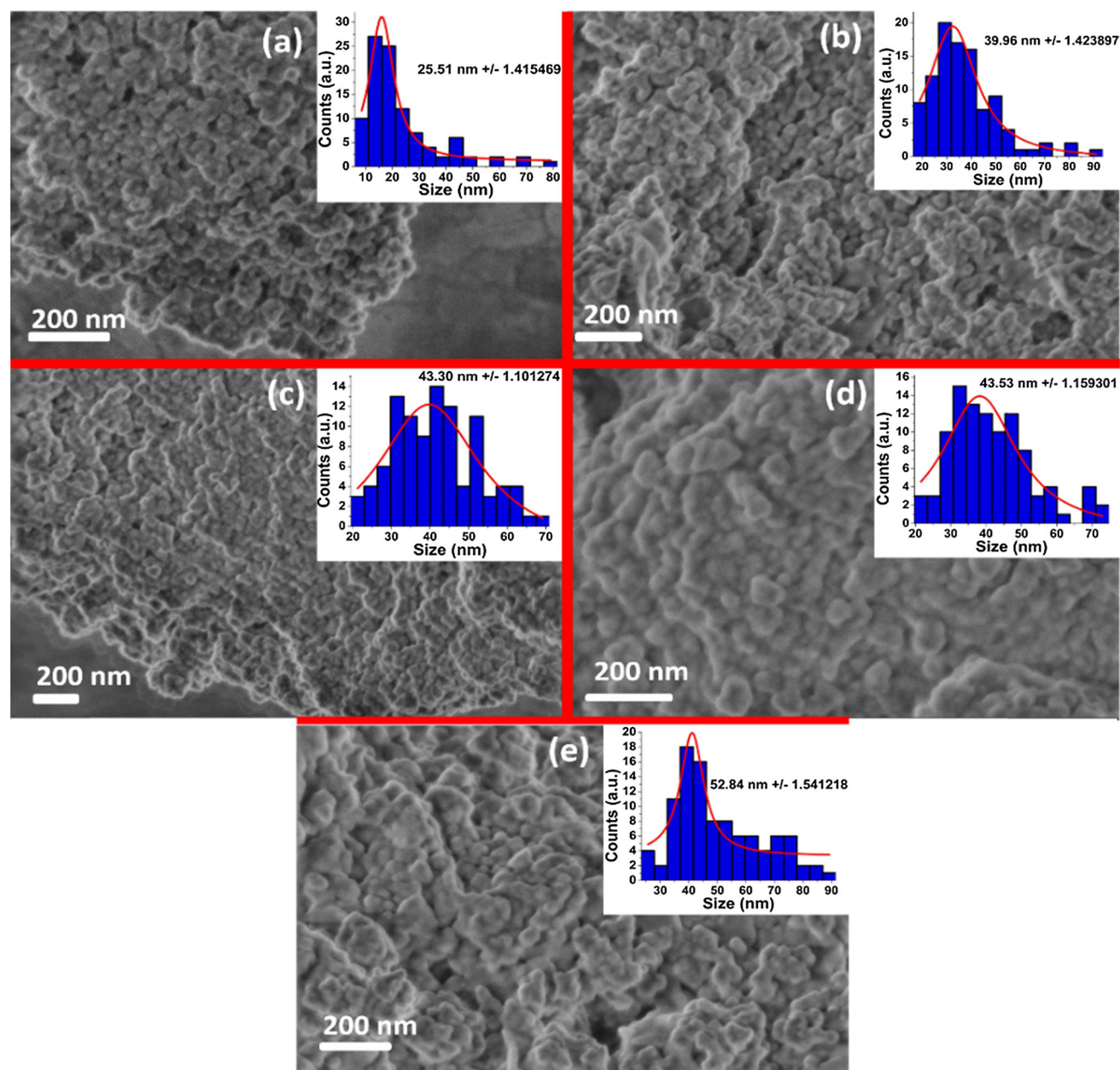


Figure 3 SEM images of NZO NPs synthesized at different AHS concentrations: **a** NZO-S0.75, **b** NZO-S1.5, **c** NZO-S3, **d** NZO-S4.5, and **e** NZO-S6. The insets show the particle size distribution of the NZO NPs calculated by using ImageJ software.

one of our co-authors in his early work demonstrated theoretically the presence of ionized OV in the band gap in the gel-combustion synthesized nanostructured NZO [19]. Valence band (VB) of the nanostructured NZO consists of O-2p orbital, whereas conduction band (CB) consists of Zr 4d and Nd 4f orbital. Based on formation energy calculation, it was inferred that ionized OV was energetically more stable than neutral oxygen vacancies. The blue and green emission bands were attributed to electronic

transitions between defect states and the conduction band, as well as impurity states at the bottom of the conduction band. The blue emission band from our NZO NPs is attributed to doubly ionized OV near CB and singly ionized OV near to VB. The green emission band is attributed to doubly ionized OV near both CB and VB [19]. However, the green band was much more intense than the blue band for the gel-combustion synthesized nanostructured NZO. In our current MSS-synthesized NZO NPs, blue emission

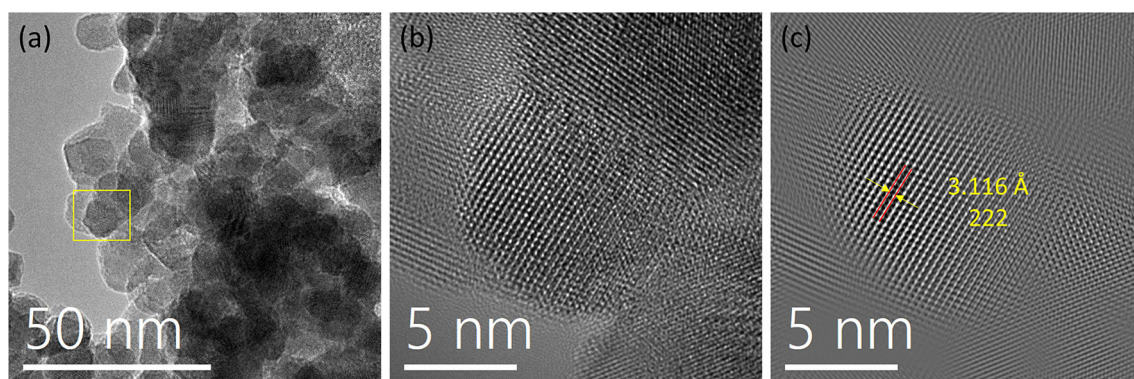


Figure 4 **a** Low-resolution TEM image, **b** high-resolution TEM (HRTEM) image and **c** corresponding filtered HRTEM image of NZO-S6 NPs. {222} facets of cubic NZO can be seen in crystalline NZO NP.

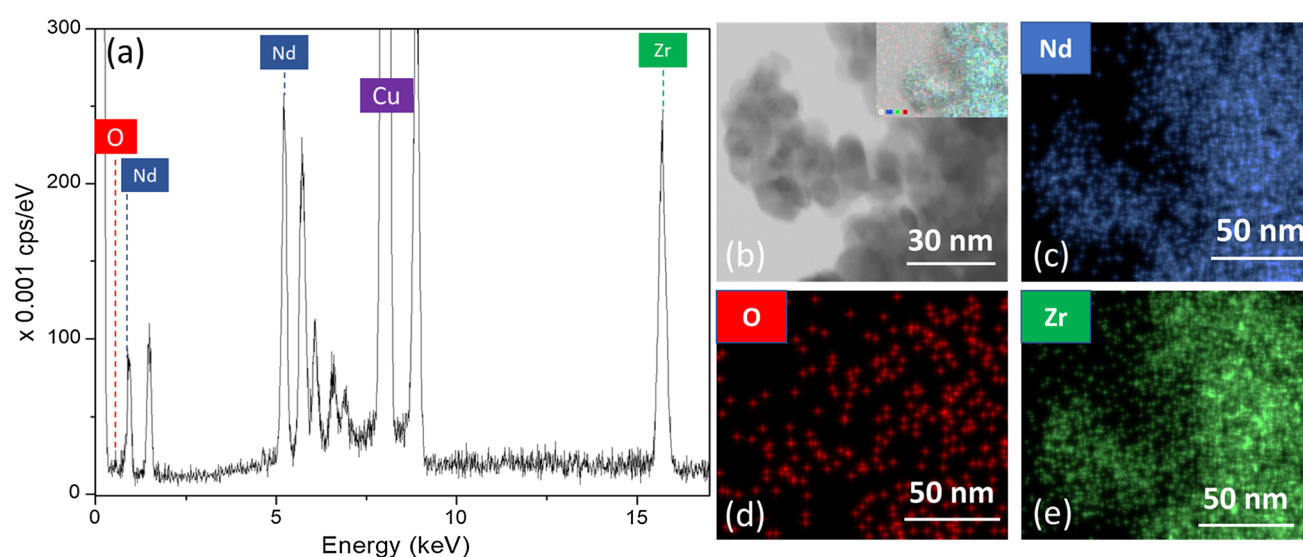


Figure 5 **a** EDS spectrum **b** scanning transmission electron micrograph (STEM) (inset: EDS composite elemental map), and **c–e** individual EDS elemental maps, confirm the presence and uniform distribution of Nd, O, and Zr in NZO NPs.

band was found to predominate over the green band. This highlights the role of synthesis method in fine-tuning the emission properties of NPs based on the application requirements. Such differences can be attributed to different energy and location of defect states in the band gap of combustion and MSS-synthesized NZO NPs. There is no perfect correlation between PL emission intensity of our NZO NPs synthesized with different NH_4OH concentrations. Initially, there is enhancement in emission intensity as the concentration of NH_4OH solution increases, which is attributed to increased particle size with less surface defects. Lowering of surface defects enhances the emission intensity because surface defects are known to provide additional pathways for non-radiative transitions. There is a dip in emission

intensity from the NZO-S4.5 NPs, which may be due to the dominant effect of hydroxyl ions over surface defect. This is a competing process which takes place as the NH_4OH concentration increases: surface defects are reduced but hydroxyl ion concentration increases [9]. These two factors have opposite effects on PL: hydroxyl ion quenches fluorescence, whereas lowering of surface defects enhances the emission intensity.

Structural evolution through in situ XRD and Raman spectroscopy

To study thermally induced phase transition, we have performed in situ XRD and Raman spectroscopy measurements. Pre-formed NZO-S6 NPs

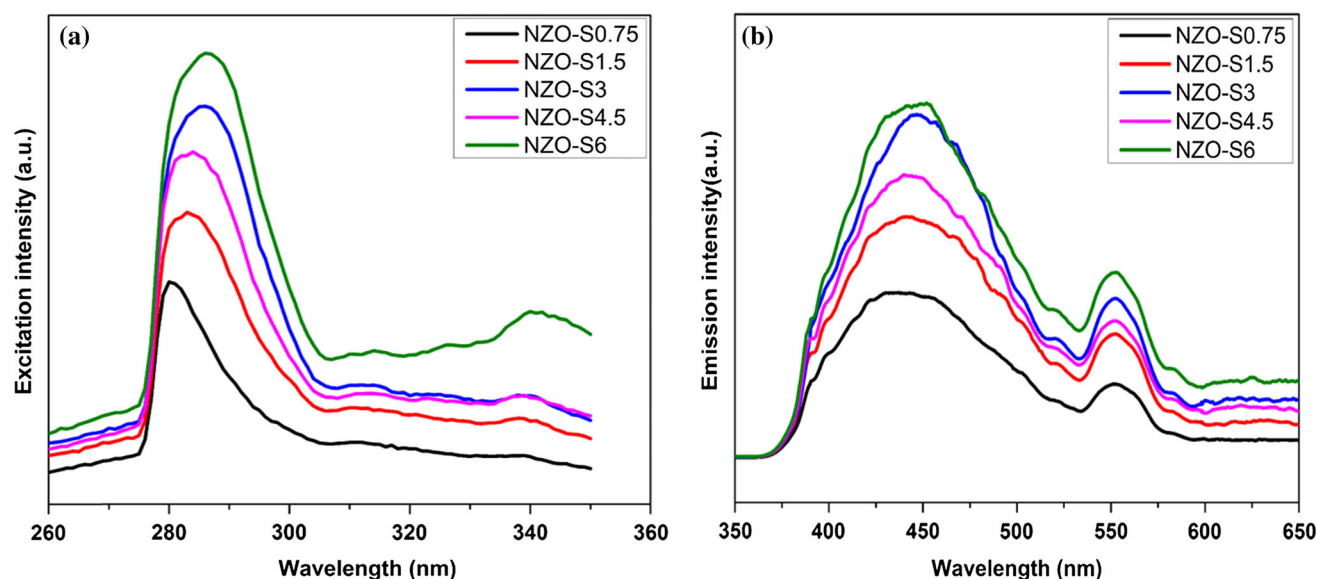


Figure 6 **a** Excitation ($\lambda_{\text{em}} = 450$ nm) and **b** emission spectra ($\lambda_{\text{ex}} = 281$ nm) of the NZO NPs prepared with different concentrations of AHS.

have shown no phase transformation through in situ XRD and Raman depicting a fluorite phase ($Fm\bar{3}m$ space group). Over the entire temperature range, XRD patterns did not show superlattice reflections of pyrochlore phase and Raman spectra displayed a single broadband characteristic of fluorite phase, unlike sextet of ideal pyrochlore structure (Fig. 7b, c, d).

The pre-formed NZO NPs were prepared with a two-step process [8, 9, 40]. Here, we took one step further to analyze possible phase transition from the coprecipitated precursor by in situ XRD (Fig. 7b). The $\text{Nd}(\text{OH})_3 \cdot \text{ZrO}(\text{OH})_2 \cdot n\text{H}_2\text{O}$ precursor was taken from the same one to synthesize the NZO-S6 NPs, and the in situ XRD measurements were taken under the same conditions with the same instrumentation. In this case, the sample remained amorphous until 898 K, and interestingly, pyrochlore phase began to evolve after 998 K. Superlattice peaks of (311), (331), (511), and (531) were detected at 1048 K and became more resolved at 1148 K. This phenomenon indicates a new design strategy of stabilizing ideal pyrochlore phase of NZO even though analogy fluorite phase is favorable based on the ionic radius ratio. Furthermore, heating from the precursor stage without any other molten salt could be a new technique to synthesize phase-selected pyrochlore NPs. However, further investigations such as morphology control and monodisperse qualities still needed in this stage

and more elusive data will come later in future investigations.

Conclusion

In this work, we have explored the structural and optical properties of $\text{Nd}_2\text{Zr}_2\text{O}_7$ nanoparticles with different sizes, which were tuned by coprecipitating NH_4OH with different concentrations prior a molten salt synthesis. X-ray diffraction and Raman spectroscopy data confirmed that the synthesized $\text{Nd}_2\text{Zr}_2\text{O}_7$ NPs were stabilized in the defect fluorite phase. Neutron diffraction patterns supported a defect fluorite structure after refinement. However, in situ XRD characterization showed a structural evolution from the precursor stage to the pyrochlore phase. Furthermore, our NZO NPs synthesized by the MSS method showed an intense photoluminescence blue band and a weak green band after excited with 281 nm, unlike samples synthesized by other methods. In addition, the higher the NH_4OH concentration, the emission output increased. Finally, all investigation corresponding in this work increased the natural understanding of phase stabilization of $\text{Nd}_2\text{Zr}_2\text{O}_7$, which provides an alternative pathway to synthesize order pyrochlore nanomaterials for multifunctional applications.

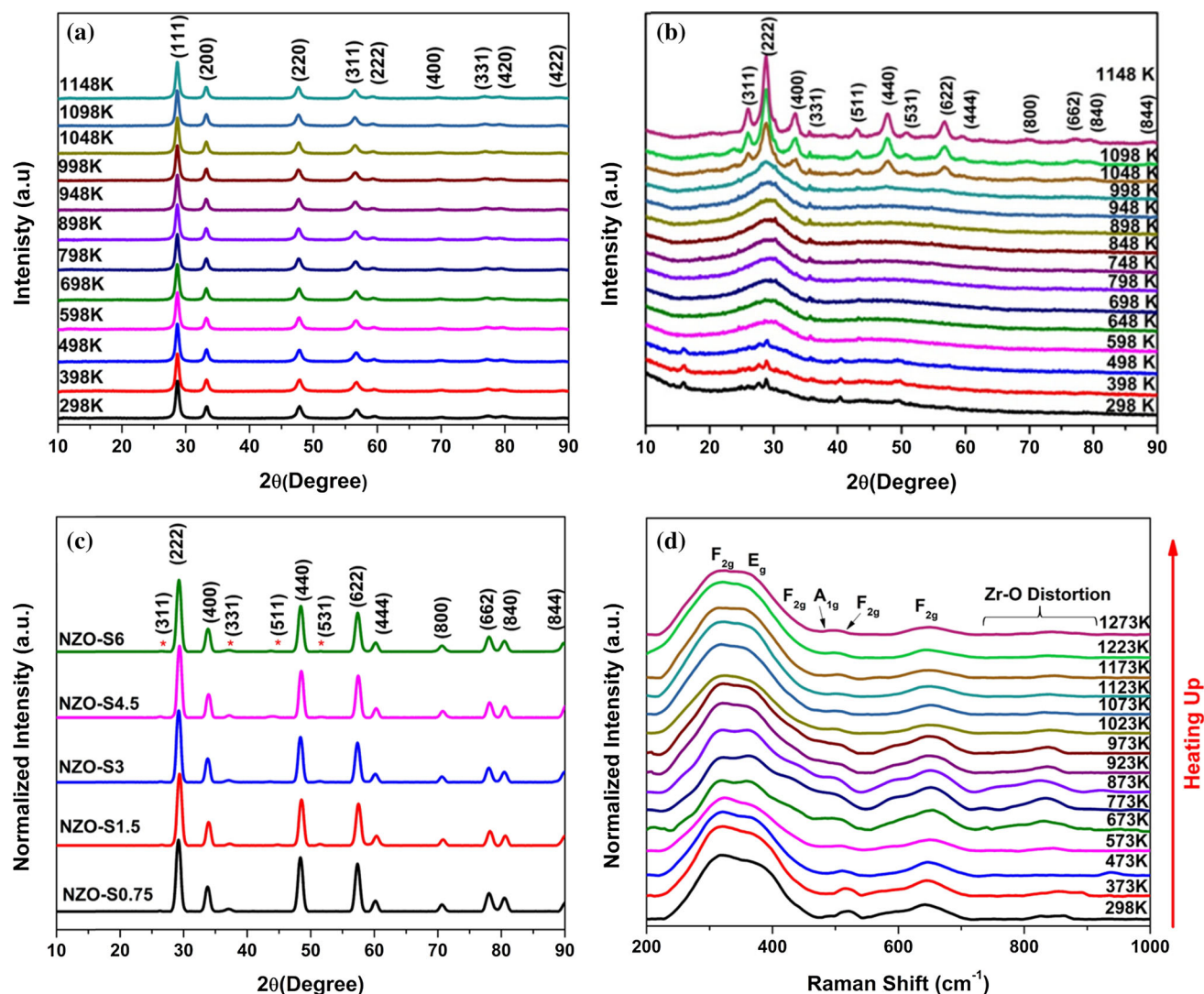


Figure 7 **a** In situ XRD patterns from the NZO-S6 NPs synthesized using MSS. **b** In situ XRD patterns of amorphous single-source complex precursor $\text{Nd}(\text{OH})_3 \cdot \text{ZrO}(\text{OH})_2 \cdot n\text{H}_2\text{O}$ coprecipitated with 6.0% NH_4OH solution concentration. **c** XRD

pattern of direct heating of single-source complex precursor at different NH_4OH concentrations. **d** In situ Raman spectra taken from direct heated $\text{Nd}(\text{OH})_3 \cdot \text{ZrO}(\text{OH})_2 \cdot n\text{H}_2\text{O}$ at 6.0% NH_4OH concentration.

Acknowledgement

The authors thank the financial support by the National Science Foundation under CHE (#1710160), DMR (#1523577), DMR (#1455154, BSG), OIA (#1355438, partial salary support for MPT), and NASA Kentucky (NNX15AK28A, MPT). The Department of Chemistry at the University of Texas Rio Grande Valley is grateful to the Robert A. Welch Foundation (Grant No. BX-0048). SKG thanks the United States-India Education Foundation (India) and the Institute of International Education (USA) for his Fulbright Nehru Postdoctoral Fellowship (# 2268/FNPDR/2017). In situ XRD and Raman measurements, TEM/

STEM and EDS characterization were conducted at the Center for Nanophase Materials Sciences, and ND data were taken at the Neutron Science Directorate, Oak Ridge National Laboratory, which is a DOE Office of Science User Facility. We also thank Dr. J. K. Keum and Dr. J. C. Neufeind for technical assistance on the in situ XRD and ND measurements.

References

- [1] Chun J, Reuvekamp PG, Chen D, Lin C, Kremer RK (2015) Promising high-k dielectric permittivity of pyrochlore-type crystals of $\text{Nd}_2\text{Hf}_2\text{O}_7$. *J Mater Chem C* 3:491–494

- [2] Zhang Y, Xie M, Zhou F, Cui X, Lei X, Song X, An S (2014) Low thermal conductivity in $\text{La}_2\text{Zr}_2\text{O}_7$ pyrochlore with A-site partially substituted with equimolar Yb_2O_3 and Er_2O_3 . *Ceram Int* 40:9151–9157
- [3] Shlyakhtina AV, Pigalskiy KS, Belov DA, Lyskov NV, Kharitonova EP, Kolbanev IV, Borunova AB, Karyagina OK, Sadovskaya EM, Sadykov VA, Ereemeev NF (2018) Proton and oxygen ion conductivity in the pyrochlore/fluorite family of $\text{Ln}_{2-x}\text{Ca}_x\text{ScMO}_{7-\delta}$ ($\text{Ln} = \text{La}, \text{Sm}, \text{Ho}, \text{Yb}$; $\text{M} = \text{Nb}, \text{Ta}$; $x = 0, 0.05, 0.1$) niobates and tantalates. *Dalton Trans* 47:2376–2392
- [4] Lu X, Shu X, Shao D, Chen S, Zhang H, Yuan X, Chi F (2018) Radiation stability of $\text{Gd}_2\text{Zr}_2\text{O}_7$ and $\text{Nd}_2\text{Ce}_2\text{O}_7$ ceramics as nuclear waste forms. *Ceram Int* 44:760–765
- [5] Mustafa GM, Atiq S, Abbas SK, Riaz S, Naseem S (2018) Tunable structural and electrical impedance properties of pyrochlores based Nd doped lanthanum zirconate nanoparticles for capacitive applications. *Ceram Int* 44:2170–2177
- [6] Cepeda-Sánchez NM, Díaz-Guillén JA, Maczka M, Amador U, Fuentes AF (2017) Mechanochemical synthesis, crystal structure and ion conduction in the $\text{Gd}_2\text{Hf}_{2-x}\text{Ti}_x\text{O}_7$ system. *J Mater Sci* 52(20):11933–11946. <https://doi.org/10.1007/s10853-017-1037-2>
- [7] Shamblin J, Tracy CL, Palomares RI, O'Quinn EC, Ewing RC, Neuefeind J, Feygenson M, Behrens J, Trautmann C, Lang M (2018) Similar local order in disordered fluorite and aperiodic pyrochlore structures. *Acta Mater* 144:60–67
- [8] Gupta SK, Zuniga JP, Abdou M, Mao Y (2018) Thermal annealing effects on $\text{La}_2\text{Hf}_2\text{O}_7:\text{Eu}^{3+}$ nanoparticles: A curious case study of structural evolution and site-specific photo- and radio-luminescence. *Inorg Chem Front* 5:2508–2521
- [9] Gupta SK, Zuniga JP, Ghosh PS, Abdou M, Mao Y (2018) Correlating structure and luminescence properties of undoped and $\text{La}_2\text{Hf}_2\text{O}_7:\text{Eu}^{3+}$ NPs prepared with different coprecipitating pH Values through experimental and theoretical studies. *Inorg Chem Front* 57:11815–11830
- [10] Abdou M, Gupta SK, Zuniga JP, Mao Y (2018) On structure and phase transformation of uranium doped $\text{La}_2\text{Hf}_2\text{O}_7$ nanoparticles as an efficient nuclear waste host. *Mater Chem Front* 2(12):2201–2211
- [11] Zuniga JP, Gupta SK, Pokhrel M, Mao Y (2018) Exploring the optical properties of $\text{La}_2\text{Hf}_2\text{O}_7:\text{Pr}^{3+}$ nanoparticles under UV and X-ray excitation for potential lighting and scintillating applications. *New J Chem* 42:9381–9392
- [12] Gupta SK, Ghosh P, Reghukumar C, Pathak N, Kadam R (2016) Experimental and theoretical approach to account for green luminescence from $\text{Gd}_2\text{Zr}_2\text{O}_7$ pyrochlore: exploring the site occupancy and origin of host-dopant energy transfer in $\text{Gd}_2\text{Zr}_2\text{O}_7:\text{Eu}^{3+}$. *RSC Adv* 6:44908–44920
- [13] Gupta SK, Reghukumar C, Kadam R (2016) Eu^{3+} local site analysis and emission characteristics of novel $\text{Nd}_2\text{Zr}_2\text{O}_7$: Eu phosphor: insight into the effect of europium concentration on its photoluminescence properties. *RSC Adv* 6:53614–53624
- [14] Gupta SK, Reghukumar C, Keskar M, Kadam R (2016) Revealing the oxidation number and local coordination of uranium in $\text{Nd}_2\text{Zr}_2\text{O}_7$ pyrochlore: a photoluminescence study. *J Lumin* 177:166–171
- [15] Gupta SK, Reghukumar C, Pathak N, Sudarshan K, Tyagi D, Mohapatra M, Pujari P, Kadam R (2017) Speciation of uranium and doping induced defects in $\text{Gd}_{1.98}\text{U}_{0.02}\text{Zr}_2\text{O}_7$: photoluminescence, X-ray photoelectron and positron annihilation lifetime spectroscopy. *Chem Phys Lett* 669:245–250
- [16] Feng T, Clarke DR, Jiang D, Xia J, Shi J (2011) Neodymium zirconate ($\text{Nd}_2\text{Zr}_2\text{O}_7$) transparent ceramics as a solid state laser material. *Appl Phys Lett* 98(15):151105
- [17] Ai L, Wang Z, Gao Y, Cui C, Wang B, Liu W, Wang L (2019) Effect of surface and bulk palladium doping on the catalytic activity of $\text{La}_2\text{Sn}_2\text{O}_7$ pyrochlore oxides for diesel soot oxidation. *J Mater Sci* 54(6):4495–4510. <https://doi.org/10.1007/s10853-018-3160-0>
- [18] Zuniga JP, Gupta SK, Pokhrel M, Mao Y (2018) Exploring the optical properties of $\text{La}_2\text{Hf}_2\text{O}_7:\text{Pr}^{3+}$ nanoparticles under UV and X-ray excitation for potential lighting and scintillating applications. *New J Chem* 42(12):9381–9392
- [19] Gupta SK, Sudarshan K, Ghosh PS, Srivastava AP, Bevara S, Pujari PK, Kadam RM (2016) Role of various defects in the photoluminescence characteristics of nanocrystalline $\text{Nd}_2\text{Zr}_2\text{O}_7$: an investigation through spectroscopic and DFT calculations. *J Mater Chem C* 4(22):4988–5000
- [20] Zinatloo-Ajabshir S, Salavati-Niasari M (2017) Photo-catalytic degradation of erythrosine and eriochrome black T dyes using $\text{Nd}_2\text{Zr}_2\text{O}_7$ nanostructures prepared by a modified Pechini approach. *Sep Purif Technol* 179:77–85
- [21] Lutique S, Konings RJM, Rondinella VV, Somers J, Wiss T (2003) The thermal conductivity of $\text{Nd}_2\text{Zr}_2\text{O}_7$ pyrochlore and the thermal behaviour of pyrochlore-based inert matrix fuel. *J Alloy Compd* 352:1–5
- [22] Guruciaga PC, Tarzia M, Ferreyra MV, Cugliandolo LF, Grigera SA, Borzi RA (2016) Field-tuned, order by disorder in frustrated ising magnets with antiferromagnetic interactions. *Phys Rev Lett* 117:167203
- [23] Wu J, Wei X, Padture NP, Klemens PG, Gell M, Garcia E, Miranzo P, Osendi MI (2002) Low-thermal-conductivity rare-earth zirconates for potential thermal-barrier-coating applications. *J Am Ceram Soc* 85:3031–3035
- [24] Payne JL, Tucker MG, Evans IR (2013) From fluorite to pyrochlore: characterisation of local and average structure of

- neodymium zirconate, $\text{Nd}_2\text{Zr}_2\text{O}_7$. *J Solid State Chem* 205:29–34
- [25] Zhao FA, Xiao HY, Bai XM, Liu ZJ, Zu XT (2018) Effects of Nd doping on the mechanical properties and electronic structures of $\text{Gd}_2\text{Zr}_2\text{O}_7$: a first-principles-based study. *J Mater Sci* 53(24):16423–16438. <https://doi.org/10.1007/s10853-018-2784-4>
- [26] Cepeda-Sánchez NM, Díaz-Guillén JA, Maczka M, Amador U, Fuentes AF (2018) Cations size mismatch versus bonding characteristics: synthesis, structure and oxygen ion conducting properties of pyrochlore-type lanthanide hafnates. *J Mater Sci* 53(19):13513–13529. <https://doi.org/10.1007/s10853-018-2402-5>
- [27] Gupta SK, Abdou M, Ghosh PS, Zuniga JP, Mao Y (2019) Thermally induced disorder-order phase transition of $\text{Gd}_2\text{Hf}_2\text{O}_7\text{:Eu}^{3+}$ nanoparticles and its implication on photo- and radioluminescence. *ACS Omega* 4(2):2779–2791
- [28] Jiang C, Stanek CR, Sickafus KE, Ueberuaga BP (2009) First-principles prediction of disordering tendencies in pyrochlore oxides. *Phys Rev B* 79(10):104203
- [29] Li Y, Kowalski PM, Beridze G, Birnie AR, Finkeldei S, Bosbach D (2015) Defect formation energies in $\text{A}_2\text{B}_2\text{O}_7$ pyrochlores. *Scripta Mater* 107:18–21
- [30] Xiao HY, Zhang FX, Gao F, Lang M, Ewing RC, Weber WJ (2010) Zirconate pyrochlores under high pressure. *Phys Chem Chem Phys* 12(39):12472–12477
- [31] Payne JL, Tucker MG, Evans IR (2013) From fluorite to pyrochlore: characterisation of local and average structure of neodymium zirconate, $\text{Nd}_2\text{Zr}_2\text{O}_7$. *J Solid State Chem* 205:29–34
- [32] Qing Q, Shu X, Shao D, Zhang H, Chi F, Lu X (2018) Irradiation response of $\text{Nd}_2\text{Zr}_2\text{O}_7$ under heavy ions irradiation. *J Eur Ceram Soc* 38(4):2068–2073
- [33] Kong L, Karatchevtseva I, Aughterson RD, Davis J, Zhang Y, Lumpkin GR, Triani G (2015) New pathway for the preparation of pyrochlore $\text{Nd}_2\text{Zr}_2\text{O}_7$ nanoparticles. *Ceram Int* 41(6):7618–7625
- [34] Bhattacharya AK, Hartridge A, Mallick KK, Woodhead JL (1994) Preparation and characterization of $\text{Ln}_2\text{Zr}_2\text{O}_7$ microspheres by an inorganic sol–gel route. *J Mater Sci* 29:6076–6078. <https://doi.org/10.1007/BF00354544>
- [35] Lee YH, Sheu HS, Kao HCI (2010) Preparation and characterization of $\text{Nd}_2\text{Zr}_2\text{O}_7$ nanocrystals by a polymeric citrate precursor method. *Mater Chem Phys* 124:145–149
- [36] Kong L, Karatchevtseva I, Gregg DJ, Blackford MG, Holmes R, Triani G (2013) $\text{Gd}_2\text{Zr}_2\text{O}_7$ and $\text{Nd}_2\text{Zr}_2\text{O}_7$ pyrochlore prepared by aqueous chemical synthesis. *J Eur Ceram Soc* 33(15):3273–3285
- [37] Kaliyaperumal C, Sankarakumar A, Palanisamy J, Paramasivam T (2018) Fluorite to pyrochlore phase transformation in nanocrystalline $\text{Nd}_2\text{Zr}_2\text{O}_7$. *Mater Lett* 228:493–496
- [38] Zhang A, Lü M, Yang Z, Zhou G, Zhou Y (2008) Systematic research on $\text{RE}_2\text{Zr}_2\text{O}_7$ (RE = La, Nd, Eu and Y) nanocrystals: preparation, structure and photoluminescence characterization. *Solid State Sci* 10:74–81
- [39] Rao KK, Banu T, Vithal M, Swamy GYSK, Kumar KR (2002) Preparation and characterization of bulk and nano particles of $\text{La}_2\text{Zr}_2\text{O}_7$ and $\text{Nd}_2\text{Zr}_2\text{O}_7$ by sol–gel method. *Mater Lett* 54:205–210
- [40] Zuniga JP, Abdou M, Gupta SK, Mao Y (2018) Molten-salt synthesis of complex metal oxide nanoparticles. *JoVE* 140:e58482
- [41] Castro AA, Morales F, Romero M, Conde- Gallardo A, Escamilla R (2018) Effect of Co partial substitution on the valence state of Ru in the $\text{Gd}_{2-x}\text{Co}_x\text{Ru}_2\text{O}_7$ pyrochlore. *J Mater Sci* 53(11):8067–8073. <https://doi.org/10.1007/s10853-018-2162-2>
- [42] Zuniga JP, Gupta SK, Abdou M, Mao Y (2018) Effect of molten salt synthesis processing duration on the photo- and radioluminescence of UV-, visible-, and X-ray-excitable $\text{La}_2\text{Hf}_2\text{O}_7\text{:Eu}^{3+}$ nanoparticles. *ACS Omega* 3(7):7757–7770
- [43] Neuefeind J, Feygenson M, Carruth J, Hoffmann R, Chipley KK (2012) The nanoscale ordered materials diffractometer NOMAD at the spallation neutron source SNS. *Nucl Instrum Methods Phys Res, Sect B* 287:68–75
- [44] Sayed FN, Grover V, Bhattacharyya K, Jain D, Arya A, Pillai C, Tyagi A (2011) $\text{Sm}_{2-x}\text{Dy}_x\text{Zr}_2\text{O}_7$ pyrochlores: probing order–disorder dynamics and multifunctionality. *Inorg Chem* 50:2354–2365
- [45] Turner KM, Rittman DR, Heymach RA, Tracy CL, Turner ML, Fuentes AF, Mao WL, Ewing RC (2017) Pressure-induced structural modifications of rare-earth hafnate pyrochlore. *J Phys: Condens Matter* 29:255401
- [46] Subramanian M, Aravamudan G, Rao GS (1983) Oxide pyrochlores—a review. *Prog Solid State Chem* 15:55–143
- [47] Mahesh SK, Rao PP, Thomas M, Francis TL, Koshy P (2013) Influence of cation substitution and activator site exchange on the photoluminescence properties of Eu^{3+} -doped quaternary pyrochlore oxides. *Inorg Chem* 52(23):13304–13313
- [48] Turner KM, Rittman DR, Heymach RA, Tracy CL, Turner ML, Fuentes AF, Mao WL, Ewing RC (2017) Pressure-induced structural modifications of rare-earth hafnate pyrochlore. *J Phys: Condens Matter* 29(25):255401
- [49] Zinatloo-Ajabshir S, Salavati-Niasari M (2017) Facile synthesis of nanocrystalline neodymium zirconate for highly efficient photodegradation of organic dyes. *J Mol Liq* 243:219–226
- [50] Klee WE, Weitz G (1969) Infrared spectra of ordered and disordered pyrochlore-type compounds in the series

- $\text{RE}_2\text{Ti}_2\text{O}_7$, $\text{RE}_2\text{Zr}_2\text{O}_7$ and $\text{RE}_2\text{Hf}_2\text{O}_7$. *J Inorg Nucl Chem* 31:2367–2372
- [51] Hagiwara T, Nomura K, Yamamura H (2014) Relationship between crystal structure and oxide-ion conduction in $\text{Nd}_2\text{Zr}_2\text{O}_7$ and $\text{La}_2\text{Zr}_2\text{O}_7$ deduced by high-temperature neutron diffraction. *Solid State Ionics* 262:551–554
- [52] Heremans C, Wuensch BJ, Stalick JK, Prince E (1995) Fast-ion conducting $\text{Y}_2(\text{Zr}_y\text{Ti}_{1-y})_2\text{O}_7$ pyrochlores: neutron Rietveld analysis of disorder induced by Zr substitution. *J Solid State Chem* 117(1):108–121
- [53] Richardson RP (2016) The thermoresponsive behaviour of selected rare-earth hafnate, zirconate, and titanate compounds. University of Witwatersrand, pp 1–162
- [54] Hudak BM, Depner SW, Waetzig GR, Talapatra A, Arroyave R, Banerjee S, Guiton BS (2017) Real-time atomistic observation of structural phase transformations in individual hafnia nanorods. *Nat Commun* 8:15316
- [55] Longo VM, Cavalcante LS, Figueiredo ATD, Santos LPS, Longo E, Varela JA, Sambrano JR, Paskocimas CA, Vicente FSD, Hernandez AC (2007) Highly intense violet-blue light emission at room temperature in structurally disordered SrZrO_3 powders. *Appl Phys Lett* 90:091906
- [56] Gupta SK, Sudarshan K, Ghosh P, Srivastava A, Bevara S, Pujari P, Kadam R (2016) Role of various defects in the photoluminescence characteristics of nanocrystalline $\text{Nd}_2\text{Zr}_2\text{O}_7$: an investigation through spectroscopic and DFT calculations. *J Mater Chem C* 4:4988–5000
- [57] Pathak N, Ghosh PS, Gupta SK, Mukherjee S, Kadam RM, Arya A (2016) An insight into the various defects-induced emission in MgAl_2O_4 and their tunability with phase behavior: combined experimental and theoretical approach. *J Phys Chem C* 120(7):4016–4031
- [58] Gupta SK, Ghosh PS, Pathak N, Arya A, Natarajan V (2014) Understanding the local environment of Sm^{3+} in doped SrZrO_3 and energy transfer mechanism using time-resolved luminescence: a combined theoretical and experimental approach. *RSC Adv* 4:29202–29215

Publisher's Note Springer Nature remains neutral with regard to jurisdictional claims in published maps and institutional affiliations.